RAPID COMMUNICATIONS

PHYSICAL REVIEW E **91**, 060401(R) (2015)

Avalanches in compressed Ti-Ni shape-memory porous alloys: An acoustic emission study

Daniel Soto-Parra,[1,2] Xiaoxin Zhang,[3] Shanshan Cao,[3] Eduard Vives,[1] Ekhard K. H. Salje,[4] and Antoni Planes[1]

[1]*Departament d'Estructura i Constituents de la Matèria, Facultat de Física, Universitat de Barcelona, Diagonal 647, E-08028 Barcelona, Catalonia, Spain*

[2]*Centro de Investigación en Materiales Avanzados. S.C. Miguel de Cervantes 120, Complejo Industrial Chihuahua. 31109 Chihuahua, Mexico*

[3]*Department of Metallic Materials Science & Engineering, School of Materials Science & Engineering, South China University of Technology, Wushan 510640, Guangzhou, People's Republic of China*

[4]*Department of Earth Sciences, University of Cambridge, Downing Street, Cambridge CB2 3EQ, United Kingdom*

(Received 3 April 2015; published 17 June 2015)

Mechanical avalanches during compression of martensitic porous Ti-Ni have been characterized by high-frequency acoustic emission (AE). Two sequences of AE signals were found in the same sample. The first sequence is mainly generated by detwinning at the early stages of compression while fracture dominates the later stages. Fracture also determines the catastrophic failure (big crash). For high-porosity samples, the AE energies of both sequences display power-law distributions with exponents $\varepsilon \simeq 2$ (twinning) and 1.7 (fracture). The two power laws confirm that twinning and fracture both lead to avalanche criticality during compression. As twinning precedes fracture, the observation of twinning allows us to predict incipient fracture of the porous shape memory material as an early warning sign (i.e., in bone implants) before the fracture collapse actually happens.

DOI: 10.1103/PhysRevE.91.060401 PACS number(s): 62.20.mm, 61.43.Gt, 81.30.Kf, 05.65.+b

I. INTRODUCTION

Scale-invariant avalanche dynamics in externally driven systems leads to power-law-distributed acoustic emission (AE) spectra whereby the avalanche exponents are expected to contain information about the process that generates AE. This idea is in contrast to mean-field approaches where the same mean-field exponents are expected for all processes [1]. There is some experimental proof that different processes can generate different avalanche sequences with different exponents because the variability of exponents between different materials may be influenced by other effects, which have nothing to do with the intrinsic dynamics of the avalanches. For instance, it is known that exponents are affected by the driving rate due to avalanche overlapping that occurs at high rates [2–4] or due to the influence of thermally activated processes in the limit of very low rates [3]. Nevertheless, there is little knowledge about systems where different mechanisms can lead to different intrinsic exponents.

In this paper we report that we have identified a classic shape-memory alloy (SMA) that displays several exponents in the same sample when produced as a porous material. This observation constitutes the ultimate proof that different exponents are obtained when one sample emits AE with two (or more) superimposed power laws that can be attributed to different collapse mechanisms. The approach is motivated by the observation that any porous SMA has (at least) two ways to respond to external stress, namely, by twinning and detwinning and by porous cavity collapse (fracture). As the porous SMA we choose Ti-Ni, which is probably the most important shape-memory alloy due to its exceptional mechanical properties and a wide range of biomedical applications [5]. It was discovered in the early 1960s [6] and has been studied intensively for more than fifty years. This alloy displays shape-memory properties related to a thermoelastic martensitic transition and has been used in many well established applications in diverse industrial fields [7]. Ti-Ni is biocompatible and thus very important for bone replacements and other medical applications. As a bone implant material it shows high strength and low elastic modulus that, for appropriate porosity, can match the elastic modulus of bones. In addition, porous Ti-Ni has been suggested as a potential high-energy absorbing material and for such purpose its mechanical properties under compression have been studied in detail [8]. In this paper we report an AE study of collapsing porous Ti-Ni under uniaxial compression. Acoustic emission measures acoustic waves associated with rapid changes of the strain field in an externally stimulated material. Detection of AE is a very sensitive technique adequate to detect local changes that occur at length scales ranging from nanometers to micrometers. It has been widely used to monitor damage in materials subjected to an external stress [9]. In this case AE essentially originates from plastic deformation, crack initiation, and propagation effects. Acoustic emission during compression of several porous minerals and synthetic glasses has been reported. In these materials, the failure event is heralded by significant precursor activity [10,11]. In the precursor regime, the mechanical response of the system to an applied compressive force has been shown not to be smooth or continuous as classically expected, but instead occurs intermittently as a sequence of jerks or avalanches arising from local fracture, which are at the origin of the AE activity. Here we combine the detection of such fracture avalanche activity with other collective changes under stress, namely, twinning and detwinning of the martensitic microstructure [12]. The statistical analysis of the energy and duration of fracture and twinning avalanches has revealed power-law behavior in both cases, which reveals that failure during compression occurs with the absence of characteristic time and length scales [13]. The paper is organized as follows. In Sec. II we describe the samples and briefly describe the experimental arrangement. Results for Ti-Ni samples of selected porosities are described and discussed in Sec. III. Finally, in Sec. IV we summarize the main conclusions of the work.

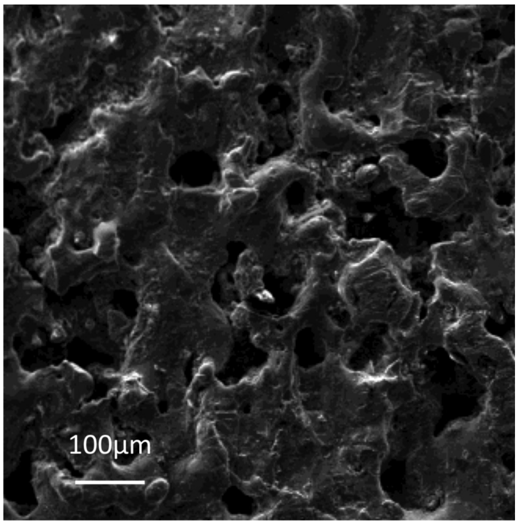

FIG. 1. A SEM image of the Ti-Ni sample showing porosity in the sample with 38.9% porosity.

II. EXPERIMENT

We have studied porous Ti-Ni samples produced by means of powder metallurgy. Nickel (60 μm, 99.9% purity) and titanium (50 μm, 99.9% purity) powders with a nominal atomic ratio of 54:46 were thoroughly blended for 24 h. This was followed by cold compaction at 50 MPa (which allows controlling the porosity) to yield a cuboid-shaped green sample of $9 \times 9 \times 25$ mm^3. Further, they were subjected to gradient sintering at 1273 K for 3 h under a protective atmosphere of flowing argon gas (99.99%). They were then cooled down to 723 K inside the furnace and aged at this temperature for 0.5 h. Finally, samples were quenched in water. The as-prepared samples were cut into small specimens of $3 \times 3 \times 4$ mm^3 for AE analysis. Porosity was determined from relative density measurements. Samples with degrees of porosity ranging from 25% to 40% were obtained. More details regarding preparation technique can be found in Ref. [14]. In all these samples a martensitic transition takes place from a cubic to a B19$'$ martensite. Transition temperatures of these samples were obtained from calorimetric measurements. These temperatures were found to be independent of porosity within experimental errors. Average values over the samples of the martensite starting temperature of the forward transition and of the ending temperature of the reverse transition are $M_s = 342.5 \pm 1$ K and $A_f = 368.5 \pm 1$ K, respectively. In Fig. 1 we show a scanning electron microscopy (SEM) image of a sample of 38.9% porosity. Pores are clearly observed with length scales ranging between 10 and 100 μm. Samples contain small amounts of impurities (identified as Ti_4Pb nanoparticles introduced from decomposition of $PbTiO_3$ and evaporation of PbO in the neighborhood during sintering) and $NiTi_2$ precipitates. The average matrix composition of the samples has been obtained from energy-dispersive x-ray spectroscopy to be about (within less than 0.5% error) 53.7 at. % Ti and 46.3 at. % Ni.

Details of the experimental arrangement for AE measurements under uniaxial compression have been described in Ref. [15]. Samples are placed between two stainless steel plates. The bottom plate is static and is hanging from the load cell at the top of the arrangement. The upper plate is pulled downward at constant force rate by guiding rods that slide along three linear ball bearings in the bottom plate. The applied force rate is experimentally controlled, which is different from most other arrangements where the controlled parameter is the displacement rate. A laser extensometer has been used to measure the vertical distance between the plates (nominal resolution of 100 nm). The applied force has been monitored with a resolution of $\sim$1 N in the range of 1 kN. Acoustic emission is detected by piezoelectric transducers embedded in the compression plates, centered at a distance of 1 mm from the sample surface. The sensors are encapsulated in stainless steel to reduce electrical noise. They are acoustically coupled with the plates by a thin layer of vaseline. The signals from the transducers are preamplified (60 dB), band filtered (between 100 kHz and 2 MHz), and transferred to an acquisition system (PCI-2, Europhysical Acoustics) working at a time resolution of 40 MHz. For the identification of signals a threshold above the instrumental noise is set. In our experiments it is fixed at 27 dB. A hit (defining an event) is assumed to start with the first crossing of this threshold. The end time of a hit is the time at which the signal voltage falls and remains below the threshold for more than a preset hit detection time (equal to 100 μs). The energy of the acoustic emission events was obtained by numerical integration of the squared voltage of signals between start and end times, divided by a reference resistance. Present experiments have been performed at low enough compression rate in order to avoid AE signal overlapping, which is known to affect the statistical analysis of the energies of AE events [3,16].

III. RESULTS AND DISCUSSION

Examples of strain vs stress curves during compression up to fracture are shown in Fig. 2. In all cases, strain depends nonlinearly on the applied stress. Deviations from linearity strongly increase when the failure point is approached. These deviations are significantly enhanced with increasing porosity. The inset of Fig. 2 shows that the failure stress decreases with increasing porosity.

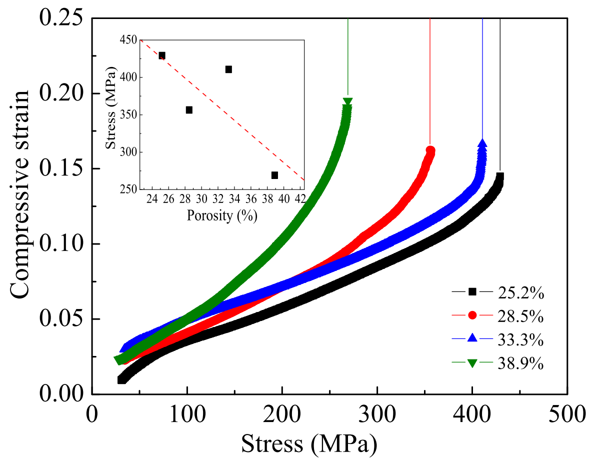

FIG. 2. (Color online) Strain-stress curves for samples of selected porosities. The vertical straight lines locate the failure stress. The inset shows the failure stress as a function of porosity. The dashed line is a linear fit.

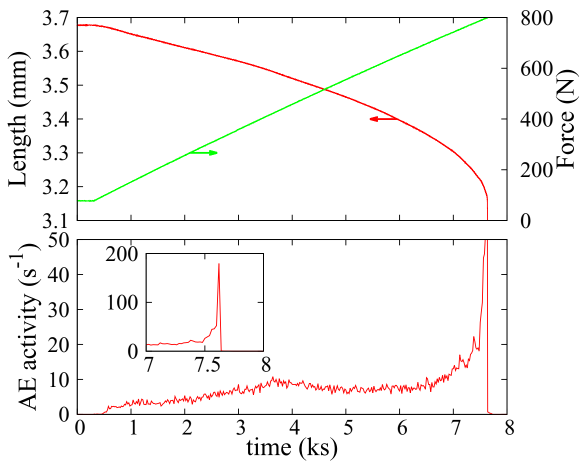

FIG. 3. (Color online) Compression experiment until failure of a sample with 38.9% porosity. The top graph shows the behavior of the sample height (left scale) and of the applied force (right scale). The bottom graph gives the AE activity as a function of time. The activity has been obtained as the number of hits measured during intervals of 20 s. The inset shows the AE activity peak close to the big crash.

In Fig. 3 we show the result of a compression experiment up to the failure point. The sample has 38.9% porosity and is in the martensitic state at room temperature. The applied force, sample length, and AE activity (number of hits measured over time intervals of 20 s) are given as a function of time. During the prefailure stages, the AE is essentially generated by detwinning effects. We have checked that by removing the applied force before failure occurs, some permanent deformation remains after complete unloading. In further loading-unloading cycling, if the maximum applied force remains below the maximum force in the first cycle, almost no AE occurs (an example is shown in Fig. 4). This permanent deformation can be erased by heating up the sample above A_f. When uniaxially compressed again at room temperature, AEs in the prefailure region are comparable to those obtained in the first run.

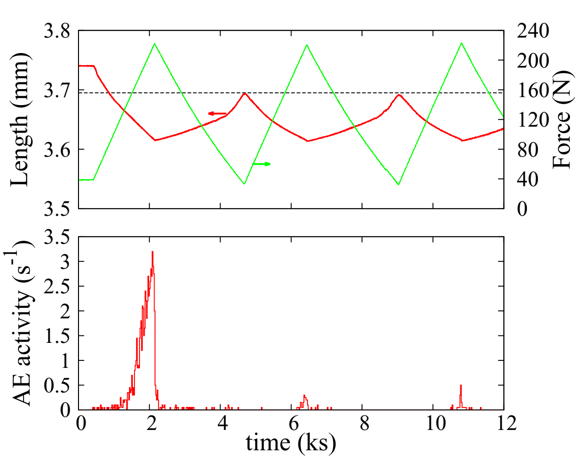

FIG. 4. (Color online) Acoustic emission activity during loading-unloading cycling up to 230 N (well below fracture collapse) corresponding to a sample with 38.9% porosity. The top panel shows force and displacement as a function of time. The dashed horizontal line indicates the length of the sample after the first loop.

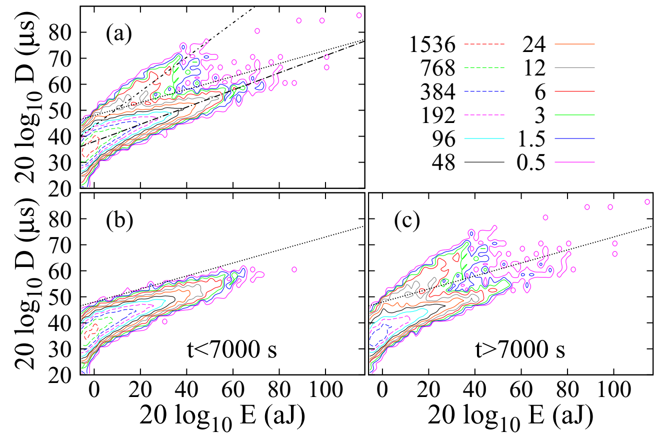

FIG. 5. (Color online) Duration versus energy frequency maps. (a) Signals recorded during the whole compression experiment shown in Fig. 3 corresponding to a sample with 38.9% porosity. The isolines correspond to regions with the same number of counts as indicated in the top right panel. (b) Signals recorded for $t < 7000$ s. (c) Signals recorded for $t > 7000$ s (failure region). The dotted line indicates the filter that has been used to separate signals of the upper and lower branches (see the text). The dashed lines in the top graph indicate the slopes corresponding to $D \sim E^{1/3}$ and $D \sim E^{2/3}$.

Figure 5(a) shows a duration D vs energy E density map (on a log-log scale) of AE signals recorded during the complete compression run up to failure as shown in Fig. 3. The isolines indicate regions with the same number of counts (as indicated in the figure). Two branches are clearly distinguished, which correspond to two different kinds of events. The lower branch corresponds to shorter duration events while the upper branch corresponds to longer duration events. Fracture seems to occur only close to the big crash. In Figs. 5(b) and 5(c) we have plotted the maps corresponding to signals recorded before the first 7000 s and after this time, respectively. The map corresponding to $t < 7000$ s displays only the lower branch, which is mainly associated with detwinning. In contrast, the map corresponding to the later stages has still the two branches, which indicates that the upper branch stems from fracture events. Both mechanisms occur simultaneously in the later stages. We can speculate that this is due to the fact that each time there is a local rupture (even small), stresses are released that can produce twinning (or detwinning) in surrounding locations. Therefore, both mechanisms may occur almost simultaneously in the late stages ($t > 7000$ s) of the compression. Only rupture is dominant at the major collapse. Note that the crest of the two branches in the frequency map can be fitted to $D \sim E^{1/3}$ and $D \sim E^{2/3}$ functions, respectively, as indicated by dashed lines in Fig. 5(a).

Samples of lowest porosity show essentially the same behavior but the number of events in the upper branch originated from the local rupture mechanism is considerably lower. In these samples, events cluster even more closely at the major collapse. In Fig. 6 duration-energy maps for samples of 25.2% and 33.3% porosity are compared with the map plotted with signals recorded during the whole compression

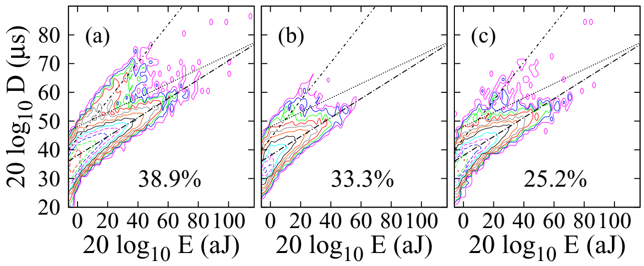

FIG. 6. (Color online) Duration versus energy frequency maps for samples of (a) 25.2%, (b) 33.3%, and (c) 38.9%. The dotted lines indicate the filter that has been used to separate signals of the upper and lower branches (see the text). They are the same for the three samples. The dashed lines in the three plots indicate the fits to the crests of the upper and lower branches, corresponding to $D \sim E^{1/3}$ and $D \sim E^{2/3}$, respectively. Contour isolines are plotted according to the legend in Fig. 5.

experiment in Fig. 5(a). It is worth noting that the same line is used in the three maps in order to separate lower and upper branches. Also, the crests of the two branches in the three maps fit reasonably well to the same functions.

Figure 7 shows the energy distributions of AE events on a log-log scale for samples of different porosities. The depicted histograms correspond to the whole set of recorded signals and to the signals that belong to the upper and lower branches in the map shown in Fig. 6(a) (separated by the dotted line). A linear behavior is obtained over more than five decades for the whole set and the lower branch signals and almost two decades for the upper branch signals, except for the sample of lower porosity (25.2%). This indicates that the corresponding distributions of energies follow power-law behavior $p(E) \sim E^{-\varepsilon}$ to a very good approximation. Note that the histograms corresponding to the whole set of data and to the lower branch are almost coincident in the three samples, which confirms that only a very small number of signals arise from fracture and occur only at the late stages of the process. A maximum-likelihood method has been used to fit the exponent ε of the distributions. This numerical technique consists of studying the behavior of the exponent ε fitted using the maximum-likelihood method as a function of a varying lower cutoff E_{min}. This analysis [17] leads to a plateau that defines the exponent (see the bottom row in Fig. 7). Fitting renders $\varepsilon = 2.0 \pm 0.1$ for signals of the lower branches (twinning and detwinning), which can be assumed to be independent of porosity within the errors. For signals of the upper branch, the power law is less well defined, especially in the sample of 25.2% porosity. This may be related to a poor statistics due to the small number of signals detected associated with local rupture mechanism. For all samples, we have checked that the energy distribution cannot be fitted with an exponential law. However, we cannot exclude that the dominant power-law behavior is affected by an exponential cutoff, which becomes more important as porosity decreases. For the sample of 38.9% the dominant power law is characterized by an exponent $\varepsilon = 1.7 \pm 0.1$, which is clearly defined over one decade. For lower porosity the fitted exponent seems to decrease, which could be interpreted in the sense that the relative probability of high-energy signals increases in this case. This is indeed consistent with the fact that fracture concentrates closer to the major event, which has a tendency to occur as a single event as porosity decreases.

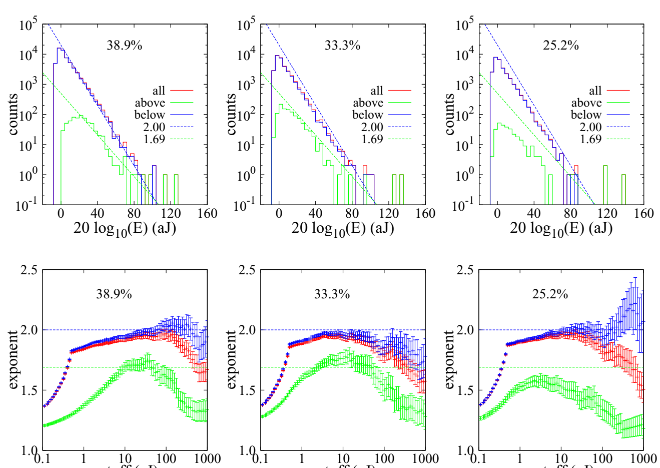

FIG. 7. (Color online) Energy distribution of AE events corresponding to all the signals (red), the signals above the filter line (green), and the signals below the filter line (blue). Dashed lines correspond to exponent values $\varepsilon = 2.00$ and 1.69. The bottom panels show likelihood plots giving the fitted exponent as a function of the cutoff energy for the three cases.

Acoustic emission signals originating from detwinning have the same values of the energy exponent expected for a martensitic transition taking place from cubic to monoclinic (as in the studied sample) [18,19]. Interestingly, the exponent $\varepsilon \simeq 1.7$ estimated for signals originating from fracture is in good agreement with values obtained during failure under compression of porous minerals such as goethite [15] or different kinds of sandstone [11] but slightly larger than the value $\varepsilon \simeq 1.4$ reported for synthetic SiO_2 porous glasses such as Vycor and Gelsil [11].

IV. CONCLUSION

We have studied AE during the uniaxial compression of the porous Ti-Ni shape-memory alloy. Two different sequences of events have been found that have been identified as detwinning and fracture, respectively. The energies of detwinning signals display a power-law distribution with a characteristic exponent that is independent of porosity. For fracture signals, the energy distribution seems to approach the power-law behavior only for samples of high enough porosity. The corresponding exponent is in agreement with the exponent reported for other porous minerals under compression. Therefore, for high porosity the criticality associated with both twinning-detwinning and fracture mechanisms occurs simultaneously during the compression process and is characterized by different critical exponents. Signals arising from fracture only occur at the very late stages of the process close to the big crash. This result suggests the possibility to predict catastrophic failure at the major collapse point from AE measurements and energy-duration analysis. We expect that these results have important implications in the use of the studied porous materials both as implant bone materials and as high-energy absorbing materials.

ACKNOWLEDGMENTS

We acknowledge financial support from the Spanish Ministry of Science (Grant No. MAT2013-40590-P). E.K.H.S. is grateful to EPSRC (Grant No. EP/K009702/1) and the Leverhulme Foundation (Grant No. RPG-2012-564) for support.

[1] E. K. H. Salje and K. A. Dahmen, Annu. Rev. Condens. Matter Phys. **5**, 233 (2014).

[2] R. A. White and K. A. Dahmen, Phys. Rev. Lett. **91**, 085702 (2003).

[3] F. J. Pérez-Reche, B. Tadić, L. Mañosa, A. Planes, and E. Vives, Phys. Rev. Lett. **93**, 195701 (2004).

[4] M. A. Lebyodkin, I. V. Shashkov, T. A. Lebedkina, K. Mathis, P. Dobron, and F. Chmelik, Phys. Rev. E **88**, 042402 (2013).

[5] K. Otsuka and X. Ren, Prog. Mater. Sci. **50**, 511 (2005).

[6] W. J. Buehler, J. V. Gilfrich, and R. C. Wiley, J. Appl. Phys. **34**, 1475 (1963).

[7] See *Science and Technology of Shape-Memory Alloys: New Developments*, edited by K. Otsuka and T. Kakeshita, special issue of MRS Bull. **27**(2) (2002).

[8] Y. Zhao, M. Taya, Y. S. Kang, and A. Kawasaki, Acta Mater. **53**, 337 (2005).

[9] M. Huang, L. Jiang, P. K. Liaw, C. R. Brooks, R. Seeley, and D. L. Klarstrom, JOM-e **50** (11) (1998).

[10] E. K. H. Salje, G. I. Lampronti, D. E. Soto-Parra, J. Baró, A. Planes, and E. Vives, Am. Mineral. **98**, 609 (2013).

[11] G. F. Nataf, P. O. Castillo-Villa, J. Baró, X. Illa, E. Vives, A. Planes, and E. K. H. Salje, Phys. Rev. E **90**, 022405 (2014).

[12] E. K. H. Salje, X. Wang, X. Ding, and J. Sun, Phys. Rev. B **90**, 064103 (2014).

[13] J. Baró, A. Corral, X. Illa, A. Planes, E. K. H. Salje, W. Schranz, D. E. Soto-Parra, and E. Vives, Phys. Rev. Lett. **110**, 088702 (2013).

[14] D. S. Li, Y. P. Zhang, G. Eggeler, and X. P. Zhang, J. Alloys Compd. **470**, L1 (2009); D. S. Li, Y. P. Zhang, X. Ma, and X. P. Zhang, *ibid.* **474**, L1 (2009).

[15] E. K. H. Salje, D. E. Soto-Parra, A. Planes, E. Vives, M. Reinecker, and W. Schranz, Philos. Mag. Lett. **91**, 554 (2011).

[16] M. A. Lebyodkin, N. P. Kobelev, Y. Bougherira, D. Entemeyer, C. Fressengeas, V. S. Gornakov, T. A. Lebedkina, and I. V. Shashkov, Acta Mater. **60**, 3729 (2012).

[17] A. Clauset, C. Shalizi, and M. Newman, SIAM Rev. **51**, 661 (2009).

[18] A. Planes, L. Mañosa, and E. Vives, J. Alloys Compd. **577**, S699 (2013).

[19] R. Niemann, J. Kopeček, O. Heczko, J. Romberg, L. Schultz, S. Fähler, E. Vives, L. Mañosa, and A. Planes, Phys. Rev. B **89**, 214118 (2014).